Optics & Laser Technology 201 (2026) 115311

Contents lists available at ScienceDirect

Optics and Laser Technology

journal homepage: www.elsevier.com/locate/optlastec

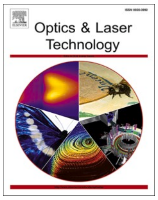

Full length article

Enhancement of wear resistance in Ti–30Zr–5Mo implants via laser cavitation peening

Ran Wang [a], Hitoshi Soyama [b], Takayoshi Nakano [c], Hideki Hosoda [d], Mitsuo Niinomi [c,e], Xiaowei Zhang [f], Deliang Zhang [a], Xiaoli Zhao [a,g,h,*]

[a] School of Materials Science and Engineering, Northeastern University, Shenyang 110819, PR China
[b] Department of Finemechanics, Tohoku University, Sendai 980-8579, Japan
[c] Division of Materials and Manufacturing Science, Graduate School of Engineering, The University of Osaka, 2-1, Yamadaoka, Suita, Osaka 565-0871, Japan
[d] Laboratory for Future Interdisciplinary Research of Science and Technology & Materials and Structures Laboratory, Institute of Integrated Research (IIR), Institute of Science Tokyo, Yokohama 226-8501, Japan
[e] Institute for Materials Research, Tohoku University, Sendai 980-8577, Japan
[f] Western Titanium Technologies Co., Ltd, Xi'an 710201, PR China
[g] National Frontiers Science Center for Industrial Intelligence and Systems Optimization, Northeastern University, Shenyang 110819, PR China
[h] Key Laboratory of Data Analytics and Optimization for Smart Industry (Ministry of Education), Northeastern University, Shenyang 110819, PR China

ARTICLE INFO

Keywords:
Laser cavitation peening without coating
Ti–30Zr–5Mo alloy
Tribological behavior
Surface oxidation
Phase transformation

ABSTRACT

In this study, laser cavitation peening without coating (LCPwC) was employed to enhance the wear resistance of Ti–30Zr–5Mo alloy for implant applications by inducing a multiscale gradient surface structure through laser–water interaction and surface oxidation. LCPwC was performed at pulse densities of 10, 50, and 100 pulses/mm^2, producing an oxide layer comprising TiO_2, Ti_2O_3, and ZrO_2. With increasing pulse density, the TiO_2 fraction decreased from 76.8% to 56.9%, whereas the Ti_2O_3 and ZrO_2 fractions increased from 6.7% to 20.9% and from 5.1% to 13.8%, respectively. The oxide layer exhibited a nanograined structure, and the average grain size decreased from 12.1 to 9.1 nm before increasing slightly to 9.5 nm, suggesting initial grain refinement followed by limited grain growth at higher pulse densities. The surface roughness increased from 0.4 μm for the untreated alloy to 1.5–4.0 μm after treatment, while the water contact angle increased from 64.9° to 121.2–130.1°, indicating increased surface hydrophobicity. The surface microhardness increased from 290 HV for the untreated alloy to 360, 392, and 403 HV after treatment, and the residual compressive stress increased in magnitude from −74 to −179 MPa. Wear testing showed that the specimen treated at 10 pulses/mm^2 exhibited improved tribological performance, with a 26.2% reduction in wear volume, a 50% reduction in wear mass, and a decrease in the coefficient of friction from 0.56 to 0.12. These improvements were mainly attributed to the formation of a protective oxide layer and the increase in surface hardness induced by LCPwC. Overall, LCPwC is an effective strategy for improving the tribological performance of Ti–30Zr–5Mo alloy and represents a promising approach for implant surface modification.

1. Introduction

Global population growth and the increasing incidence of trauma- and tumour-related disorders have intensified the clinical demand for effective treatments of musculoskeletal diseases, including osteoporosis and arthropathy. Artificial bone implants provide effective solutions for repairing bone defects, with titanium (Ti) and its alloys being preferred materials due to their high specific strength, low elastic modulus, non-magnetic properties, excellent biocompatibility, and superior corrosion resistance [1]. Zirconium (Zr), a group IV element similar to Ti, enhances alloy performance through solid solution strengthening and complete solubility with Ti, while suppressing undesirable phase precipitation [2]. The high oxidation sensitivity of Ti and Zr promotes the formation of a dense oxide film on alloy surfaces, further improving corrosion resistance [3,4]. Molybdenum (Mo), a potent β-phase stabilizer, enhances hardness and significantly reduces the elastic modulus even at low concentrations [5]. Consequently, Ti–Zr–Mo alloys with high Zr content show great promise for biomedical applications,

---

* Corresponding author at: School of Materials Science and Engineering, Northeastern University, Shenyang 110819, PR China.
E-mail address: zhaoxl@mail.neu.edu.cn (X. Zhao).

https://doi.org/10.1016/j.optlastec.2026.115311
Received 11 December 2025; Received in revised form 7 April 2026; Accepted 12 April 2026

particularly in load-bearing implants [6–12].

Material failure often initiates at the surface, necessitating advanced surface modification techniques to improve the mechanical properties and surface-related biological performance of titanium alloys for demanding biomedical applications [13]. Surface modification techniques such as shot peening, nitrogen ion implantation, and laser shock peening (LSP) have been extensively investigated for improving the surface performance of titanium alloys. For instance, Wang et al. [14] improved the fatigue performance of TA15 titanium alloy through shot peening and nitrogen ion implantation, while Nair et al. [15] employed laser shock peening without coating (LPwC) to enhance the biocorrosion resistance of Ti–6Al–7Nb (wt.%) alloy in simulated body fluid. Similarly, Luo et al. [16] and Zhu et al. [17] reported that LSP significantly improved the hardness and wear resistance of stainless steel and bearing steel, respectively. However, limitations such as oxide-film cracking induced by thermal stress [18] and excessive surface roughness after treatment [19,20] underscore the need for surface modification methods that are both milder and more precise.

Laser cavitation peening (LCP) is an emerging surface-strengthening technique that relies on pressure waves and microjets generated by the collapse of cavitation bubbles in a liquid medium [21]. Unlike conventional shot peening, LCP may reduce excessive surface roughening and material damage, making it attractive for biomedical implant surface modification. Previous studies have demonstrated the effectiveness of LCP in improving the surface integrity of magnesium alloys [22], Q235 steel [23], and grey cast iron [24]. However, for titanium alloys, the application of LCP remains relatively limited. Kuji et al. [25] and Soyama et al. [26] reported improved surface integrity and fatigue life in Ti–6Al–4 V alloy after underwater LCP, while Zhang et al. [27] and Ren et al. [28] showed that laser energy influenced residual stress, hardness, and plastic deformation depth. These findings highlight the versatility of LCP; however, its application to high-zirconium Ti–Zr–Mo alloys remains underexplored, particularly with respect to their unique oxidation behavior.

In this study, laser cavitation peening without coating (LCPwC) is defined as a laser-based surface treatment performed in water without any protective coating, enabling direct laser–water–metal interaction. LCPwC is of particular interest for Ti–Zr–Mo alloys because of the high oxidation sensitivity of Ti and Zr. Unlike coating-assisted methods, LCPwC enables direct interaction between the laser-induced cavitation field and the alloy surface, thereby promoting the in situ formation of a ceramic oxide layer. This oxide layer, combined with the induced residual compressive stress, is expected to enhance surface hardness and wear resistance. It may also influence surface-related biological responses and help overcome the limitations of conventional surface treatments that can compromise surface integrity or increase roughness. Tailoring the pulse density in LCPwC may regulate the composition and distribution of the oxide layer, providing a potential route to improve the mechanical performance of titanium alloys for biomedical applications.

This study investigates the effects of LCPwC on a high-zirconium Ti–30Zr–5Mo alloy, with particular emphasis on the composition, morphology, microstructure, and mechanical properties of the surface oxide layer. By employing three distinct pulse densities, we investigate the relationships among residual compressive stress, hardness enhancement, oxide-layer formation, and wear resistance. This work addresses an important gap in understanding the effects of LCP on oxidizable titanium alloys and provides insights into optimizing their surface performance for biomedical implant applications.

2. Experimental procedure

2.1. Materials

The experimental material was a wrought Ti–30Zr–5Mo (wt.%) alloy, selected for its high zirconium content, which facilitated the in situ formation of an oxide layer during LCPwC. Rectangular specimens with dimensions of 40 mm × 32 mm × 6 mm were prepared. The LCPwC treatment was applied to designated surface areas at different pulse densities, as illustrated in Fig. 1(a–c). To optimize cavitation efficiency and minimize surface irregularities that could scatter laser energy or impede the formation of the oxide layer, all specimen surfaces were sequentially ground using SiC abrasive papers of 800, 1200, 1500, and 2000 grit to a smooth finish ($R_a < 0.1$ μm). The specimens were then ultrasonically cleaned in ethanol for 10 min to remove grinding residues and contaminants, ensuring a pristine surface for LCPwC processing.

2.2. Laser cavitation peening without coating process

Laser cavitation peening without coating (LCPwC) was conducted using a Q-switched Nd:YAG laser (Continuum, San Jose, CA, USA) with a wavelength of 1064 nm, pulse energy of 0.35 J, pulse width of 6 ns, beam diameter of 6 mm, and repetition rate of 10 Hz. The experimental setup is illustrated in Fig. 1(d). The laser beam was directed by mirrors, expanded through a concave lens, and then focused by a convex lens with a focal length of 100 mm into a quartz chamber (150 mm × 150 mm × 150 mm) filled with deionized water. The chamber wall thickness was 3 mm to minimize laser-induced damage. The water was circulated at a flow rate of 5 L/min to remove ablation-generated particles, and degassing was performed using a vacuum pump to minimize the buffering effect during cavitation bubble collapse. All experiments were conducted at atmospheric pressure and room temperature (25 °C). The specimens were positioned approximately 20 mm below the water surface to promote cavitation effects and oxide-layer formation on the Ti–30Zr–5Mo alloy surface. The laser followed a Z-shaped scanning path with a 50% overlap rate, as shown in Fig. 1(e), to ensure uniform treatment. Pulse densities of 10, 50, and 100 pulses/mm^2, corresponding to the macroscopic morphologies shown in Fig. 1(a–c), were achieved by adjusting the scanning speed.

2.3. Oxide layer characterization

To facilitate detailed analysis of the surface oxide layer and the mechanical properties of LCPwC-treated Ti–30Zr–5Mo alloy, the specimens were sectioned to dimensions suitable for each characterization technique. A schematic illustration of the processed surface microstructure for oxide-layer characterization and microhardness measurement is shown in Fig. 1(f). Phase constituents of the oxide layer were determined using a SmartLab X-ray diffractometer (XRD, Rigaku, Japan) with Cu K_α radiation ($\lambda = 1.5406$ Å, 40 kV, 40 mA, step size 0.02°, scan rate 5°/min). Cross-sectional morphology and oxide-layer thickness were examined using a JEOL JSM-7001F scanning electron microscope (SEM) operated at an accelerating voltage of 15 kV for specimens treated at pulse densities of 10, 50, and 100 pulses/mm^2, corresponding to the conditions shown in Fig. 1(a–c). Electron backscatter diffraction (EBSD, Bruker e-Flash FS detector) was performed with a step size of 0.5 μm to analyze phase content and kernel average misorientation (KAM), which was used to assess local strain and dislocation density.

Surface chemical composition and valence states of the oxide layer were characterized using a PHI Quantera II X-ray photoelectron spectrometer (XPS, Japan) equipped with an Al K_α X-ray source ($h\nu = 1486.6$ eV). Surface morphology and roughness (S_a) were measured using a Zeiss LSM900 ultra-high-resolution confocal microscope. Surface wettability was assessed using an OCA15EC video-optical contact angle measuring instrument with deionized water droplets. Residual stress was measured using a DST-17 X-ray stress analyzer based on the $\sin^2\psi$ method, with the (213) diffraction plane selected over a scanning angle range of 130°–140°. Measurements were repeated three times at each point to ensure accuracy and consistency. Microhardness was measured using a 401MVD$^{\text{TM}}$ Vickers hardness tester with a 10 g load and 15 s dwell time. Hardness measurements were performed on untreated and LCPwC-treated specimens (10, 50, and 100 pulses/mm^2) along cross-

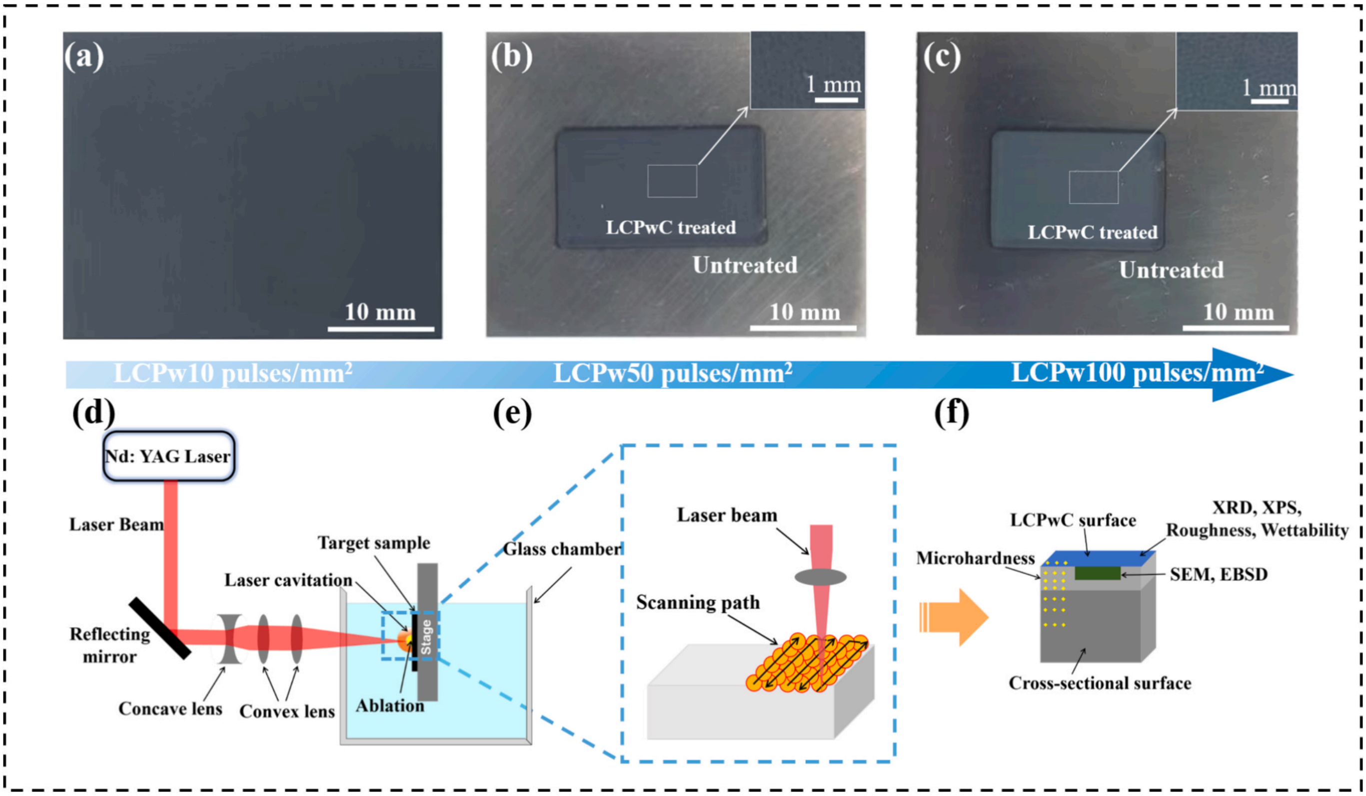

Fig. 1. (a–c) Macroscopic morphology of the Ti–30Zr–5Mo alloy surfaces after LCPwC at different pulse densities: (a) 10 pulses/mm^2, (b) 50 pulses/mm^2, and (c) 100 pulses/mm^2; (d) schematic of the LCPwC setup illustrating the laser beam path, water chamber, and specimen position; (e) Z-shaped scanning path with a 50% overlap rate for uniform surface treatment of the Ti–30Zr–5Mo alloy; and (f) schematic of the processed surface microstructure for oxide-layer characterization and microhardness measurement.

sectional depth profiles to evaluate hardness gradients associated with the oxide layer and subsurface deformation.

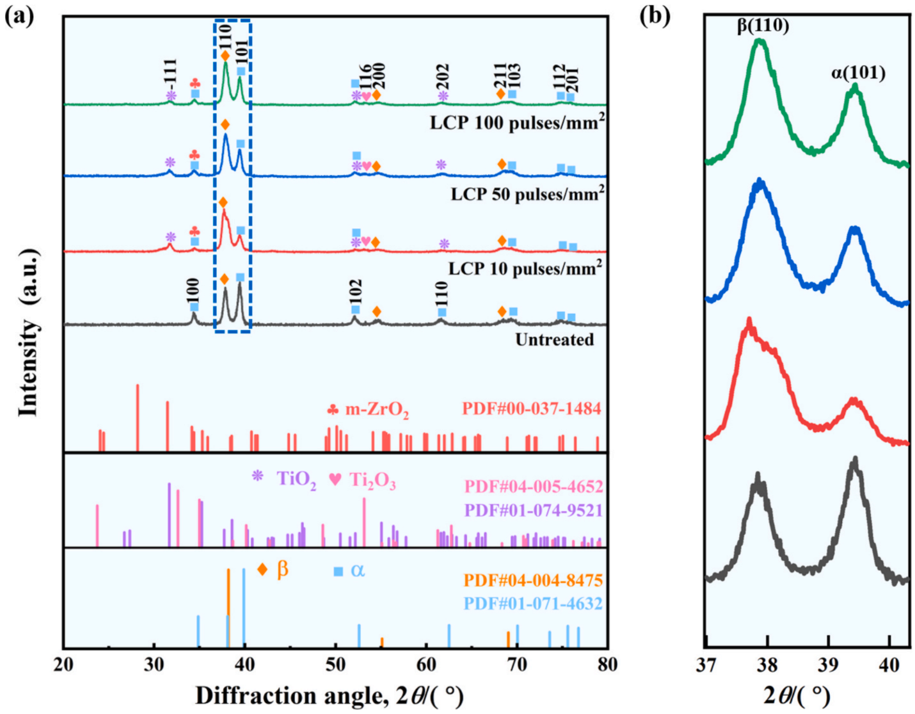

Fig. 2. (a) XRD patterns of the untreated and LCPwC-treated Ti–30Zr–5Mo alloy at pulse densities of 10, 50, and 100 pulses/mm^2; (b) magnified XRD patterns of the α{101} and β{110} peaks, highlighting the α → β phase transformation and peak shifts.

2.4. Friction and wear tests

Friction and wear tests were conducted using an Optimal SRV5 tester, with a SiC ball (10 mm in diameter) serving as the counterface and reciprocating against the Ti–30Zr–5Mo alloy surface. Test specimens measuring 10 mm × 10 mm × 6 mm were prepared as follows: specimens treated with LCPwC at a pulse density of 10 pulses/mm^2, corresponding to the condition shown in Fig. 1(a), were tested with the oxide layer retained in the as-treated condition. In contrast, untreated specimens were ground with 3000-grit SiC abrasive paper, followed by polishing with 1 μm diamond paste to achieve a mirror-finished surface ($R_a < 0.05$ μm). All specimens were ultrasonically cleaned in ethanol for 10 min to remove contaminants. Tests were performed in ambient air (25 °C, 50% relative humidity) with a normal load of 2 N, a linear reciprocating frequency of 1 Hz, a stroke length of 3 mm, and a duration of 60 min. Mass was measured before and after testing using an analytical balance with a resolution of 0.0001 g to determine the mass loss. Wear track morphology was analyzed using scanning electron microscopy (SEM) and confocal microscopy, as described in Section 2.3, to correlate surface features with wear performance.

3. Results

3.1. Microstructural and phase analysis

As shown in Fig. 2, after LCPwC, the intensity of the β{110} peak increases. In contrast, the intensity of the α{101} peak decreases significantly, indicating an α → β phase transformation in the surface layer [29]. In addition, oxide phases, including TiO_2, Ti_2O_3, and ZrO_2, are identified, and the intensity of the TiO_2{111} peak increases as the pulse density increases. The full width at half maximum (FWHM) of the TiO_2{111} peak increases by 33.4% as the pulse density increases from 10 to 50 pulses/mm^2 and by 27.9% from 50 to 100 pulses/mm^2, suggesting grain refinement and increased microstrain within the oxide layer [30].

The average subgrain size and microstrain of the oxide layer are estimated using the Scherrer and Wilson equations [31].

$$D = \frac{K\lambda}{\beta\cos\theta} \tag{1}$$

$$\varepsilon \approx \frac{\beta}{4\tan\theta} - \frac{K\lambda}{D\cos\theta} \tag{2}$$

where D is the average grain size, ε is the microstrain, K is the crystallite shape factor ($K = 0.9$ for Ti), λ is the X-ray wavelength, θ is the Bragg angle, and β is the FWHM of the diffraction peak. The average grain sizes of the oxide layer are calculated to be 12.1 nm at 10 pulses/mm^2, 9.1 nm at 50 pulses/mm^2, and 9.5 nm at 100 pulses/mm^2, indicating initial grain refinement followed by slight grain growth at higher pulse densities. This trend may result from defect accumulation reaching saturation at high pulse densities, which limits nucleation, while stress-driven recovery and surface oxidation may promote limited local grain growth. Microstrain increases with pulse density, suggesting enhanced lattice distortion associated with residual stresses, as evidenced by a shift in the β{110} peak from 31.79° to 31.81° (Fig. 2(b)) [32].

As shown in Fig. 3(a–f), oxide layers are observed on the surfaces of

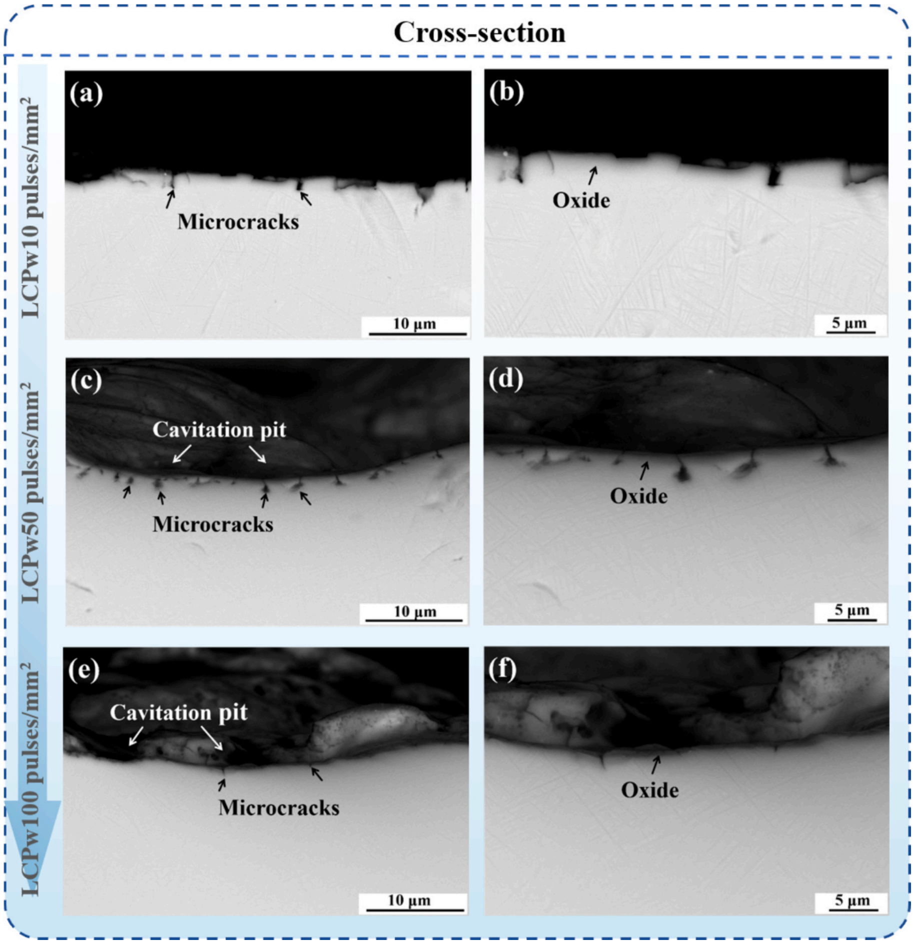

Fig. 3. Cross-sectional SEM images of the Ti–30Zr–5Mo alloy after LCPwC treatment at different pulse densities: (a, b) 10 pulses/mm^2, (c, d) 50 pulses/mm^2, and (e, f) 100 pulses/mm^2, showing oxide layers, micropits, and surface cracks.

LCPwC-treated specimens [15]. Micropits and surface cracks are observed, particularly at 50 pulses/mm^2 (Fig. 3(c)), and are attributed to shock waves and high-speed jets generated during cavitation collapse, which induce localized plastic deformation. The oxide-layer thickness, measured from SEM cross-sectional images, decreases from 3.9 μm at 10 pulses/mm^2 to 2.4 μm at 50 pulses/mm^2 and 1.3 μm at 100 pulses/mm^2. This thinning may result from the higher pulse density, which delivers intense energy in shorter intervals, thereby elevating transient surface temperatures while reducing cooling time and limiting oxygen diffusion and oxide growth. More intense cavitation at higher pulse densities may also remove nascent oxide, further reducing film thickness [25]. The thinner and denser oxide layer may contribute to improved mechanical stability by suppressing crack propagation.

EBSD analysis, as shown in Fig. 4, reveals microstructural changes in the Ti–30Zr–5Mo alloy induced by LCPwC treatment at increasing pulse densities. At 10 pulses/mm^2, grain boundaries are predominantly low-angle (2–15°), with an average KAM value of 0.72°, indicating moderate local strain. KAM values increase to 0.76° at 50 pulses/mm^2 and 0.80° at 100 pulses/mm^2, reflecting higher plastic strain and dislocation density. The geometrically necessary dislocation (GND) density, calculated from KAM, rises from 7.5×10^{14} m^{-2} at 10 pulses/mm^2 to 7.6×10^{14} m^{-2} at 50 pulses/mm^2 and 8.1×10^{14} m^{-2} at 100 pulses/mm^2, indicating progressive dislocation accumulation. KAM maps (Fig. 4 (d–f)) reveal elevated misorientation near low-angle grain boundaries (LAGBs), indicating strain localization and dislocation pile-up that hinder further dislocation slip [33]. EBSD phase maps indicate an increase in β-phase content with pulse density, which may be associated with repeated shock loading and transient adiabatic heating that facilitate α → β phase transformation.

Overall, the results suggest that LCPwC treatment at different pulse densities refines the grains, increases microstrain, and promotes the α → β phase transformation in the Ti–30Zr–5Mo alloy. Together, the thinner and denser oxide layer and the enhanced dislocation density indicate significant microstructural modification, thereby providing a basis for optimizing the surface performance of the alloy for load-bearing biomedical applications.

3.2. Surface oxidation state

To investigate the effect of LCPwC on the surface oxidation behavior of the Ti–30Zr–5Mo alloy, XPS analysis is performed on the LCPwC-treated specimens. As shown in Fig. 5, the survey spectra (Fig. 5(a)) show Ti, Zr, Mo, O, and trace C (attributed to adventitious carbon) on the surfaces of all LCPwC-treated specimens. The relative fraction of TiO_2 decreases from 76.8% at 10 pulses/mm^2 to 56.9% at 100 pulses/mm^2, while that of Ti_2O_3 increases from 6.7% to 20.9% (Fig. 5(b)). A

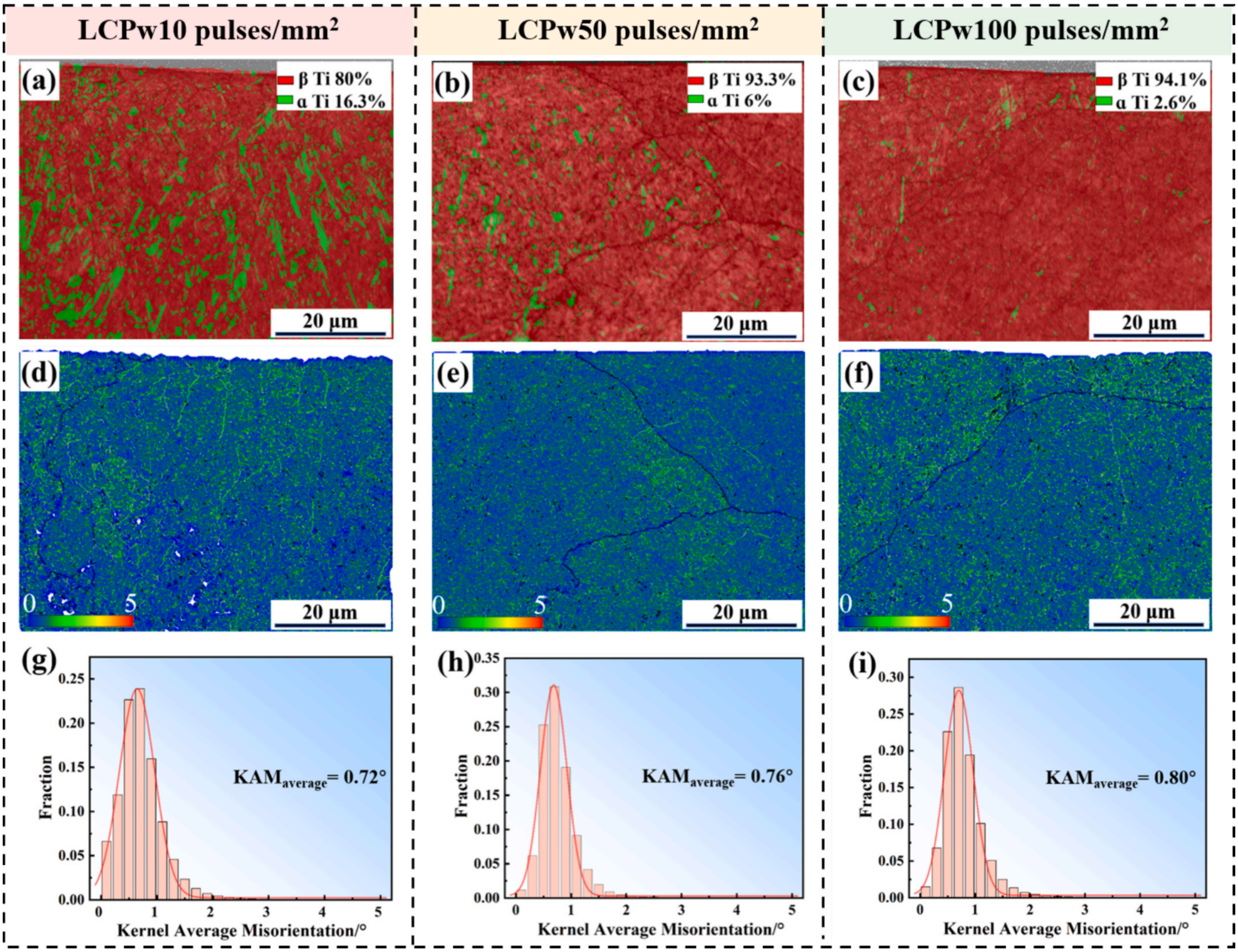

Fig. 4. EBSD analysis of the LCPwC-treated Ti–30Zr–5Mo alloy at pulse densities of (a, d, g) 10 pulses/mm^2, (b, e, h) 50 pulses/mm^2, and (c, f, i) 100 pulses/mm^2. Subfigures show (a–c) phase maps, (d–f) KAM maps, and (g–i) grain boundary distributions, highlighting increased β-phase content and strain localization with increasing pulse density.

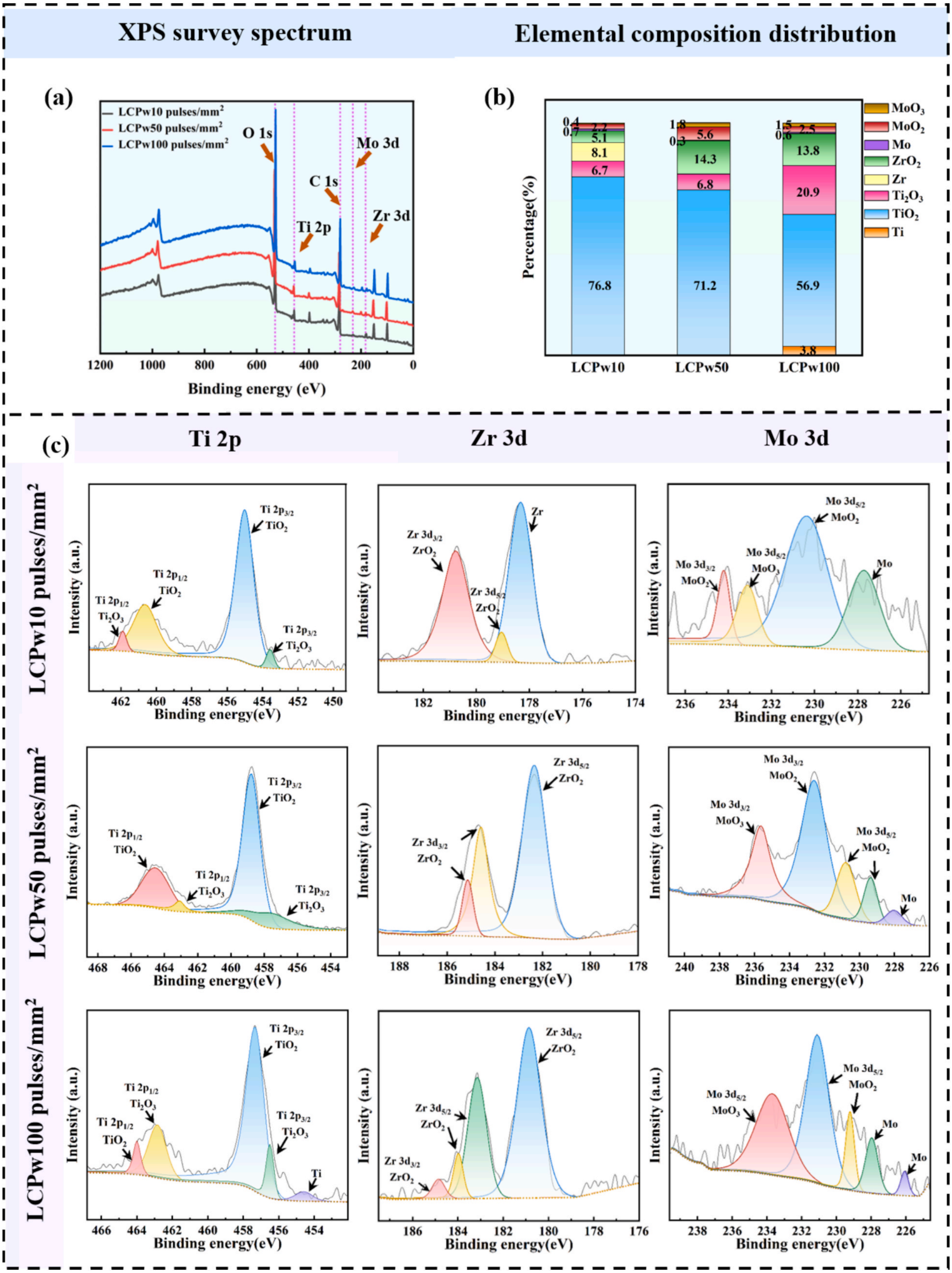

Fig. 5. XPS analysis of the Ti–30Zr–5Mo alloy surfaces: (a) survey spectra of the LCPwC-treated specimens, showing Ti, Zr, Mo, O, and C peaks; (b) percentage distribution of oxide species (TiO_2, Ti_2O_3, ZrO_2, MoO_3, and MoO_2) at varying pulse densities; and (c) high-resolution spectra of Ti 2p, Zr 3d, and Mo 3d, highlighting valence-state changes with increasing pulse density.

metallic Ti^0 peak at 454.3 eV (3.8% relative content) emerges at 100 pulses/mm^2, suggesting a relatively oxygen-deficient environment. These changes suggest that a higher pulse density promotes the formation of lower-valence oxides owing to intense cavitation-induced shock waves and transiently elevated temperatures, which may limit oxygen availability for complete oxidation.

The Zr 3d spectra reveal a dominant Zr^{4+} state (ZrO_2), with increased peak intensity at higher pulse densities, suggesting enhanced Zr oxidation. The Mo 3d spectra exhibit Mo^{6+} (MoO_3), Mo^{4+} (MoO_2), and metallic Mo, with MoO_2 content increasing at higher pulse densities, suggesting a greater tendency toward low-valence oxides under intense LCPwC conditions. Cavitation jets and thermomechanical effects at higher pulse densities may remove nascent oxides and limit oxygen diffusion, thereby contributing to the formation of a thinner, heterogeneous oxide layer with mixed-valence states.

3.3. Surface morphology and roughness

Surface morphology and roughness are important surface characteristics that influence the mechanical performance of Ti–30Zr–5Mo alloy implants and may also affect their biological response [34]. LCPwC induces severe plastic deformation and cavitation erosion, altering surface topography and increasing roughness. While increased roughness may reduce the strengthening effect [24], it may also influence osteoblast adhesion and osseointegration in bone-fixation applications [35]. The three-dimensional surface morphology and line profiles of the untreated and LCPwC-treated specimens are analyzed using an ultra-high-resolution confocal microscope, as shown in Fig. 6(a–d). LCPwC-treated surfaces exhibit peaks, valleys, micropits, and craters, which are attributed to laser ablation and cavitation-induced shock waves, consistent with SEM observations (Fig. 3(a–f)) [36]. The arithmetic mean roughness (S_a) increases from 0.4 μm (untreated) to 1.5 μm at 10 pulses/mm^2, 4.0 μm at 50 pulses/mm^2, and 3.7 μm at 100 pulses/mm^2. The initial increase in roughness may result from intensified cavitation and micropit formation, while the slight decrease at 100 pulses/mm^2 may be attributed to oxide-layer thinning and surface smoothing caused by stronger cavitation jets removing nascent oxides, as observed in SEM and XPS analyses (Figs. 3, 5) [24,37].

3.4. Wettability

Surface wettability, which may influence biological responses, is assessed using the static contact angle method, as shown in Fig. 7(a) [38]. The water contact angle increases from 64.9° for the untreated specimen to 121.2° at 10 pulses/mm^2, 124.5° at 50 pulses/mm^2, and 130.1° at 100 pulses/mm^2, indicating progressively enhanced hydrophobicity after LCPwC treatment with increasing pulse density. This trend correlates with the increased roughness (Fig. 6(a–d)), which reduces the effective contact area between the water droplet and the surface, resulting in a more spherical droplet shape [39]. In addition, the heterogeneous oxide layer formed during LCPwC in water, including Ti_2O_3 and ZrO_2 (Fig. 5), may alter the surface free energy, further contributing to the increase in hydrophobicity [40,41]. Although hydrophilicity is often considered beneficial for osteoblast adhesion [35], the increase in hydrophobicity observed after LCPwC may affect subsequent biological interactions and therefore warrants further

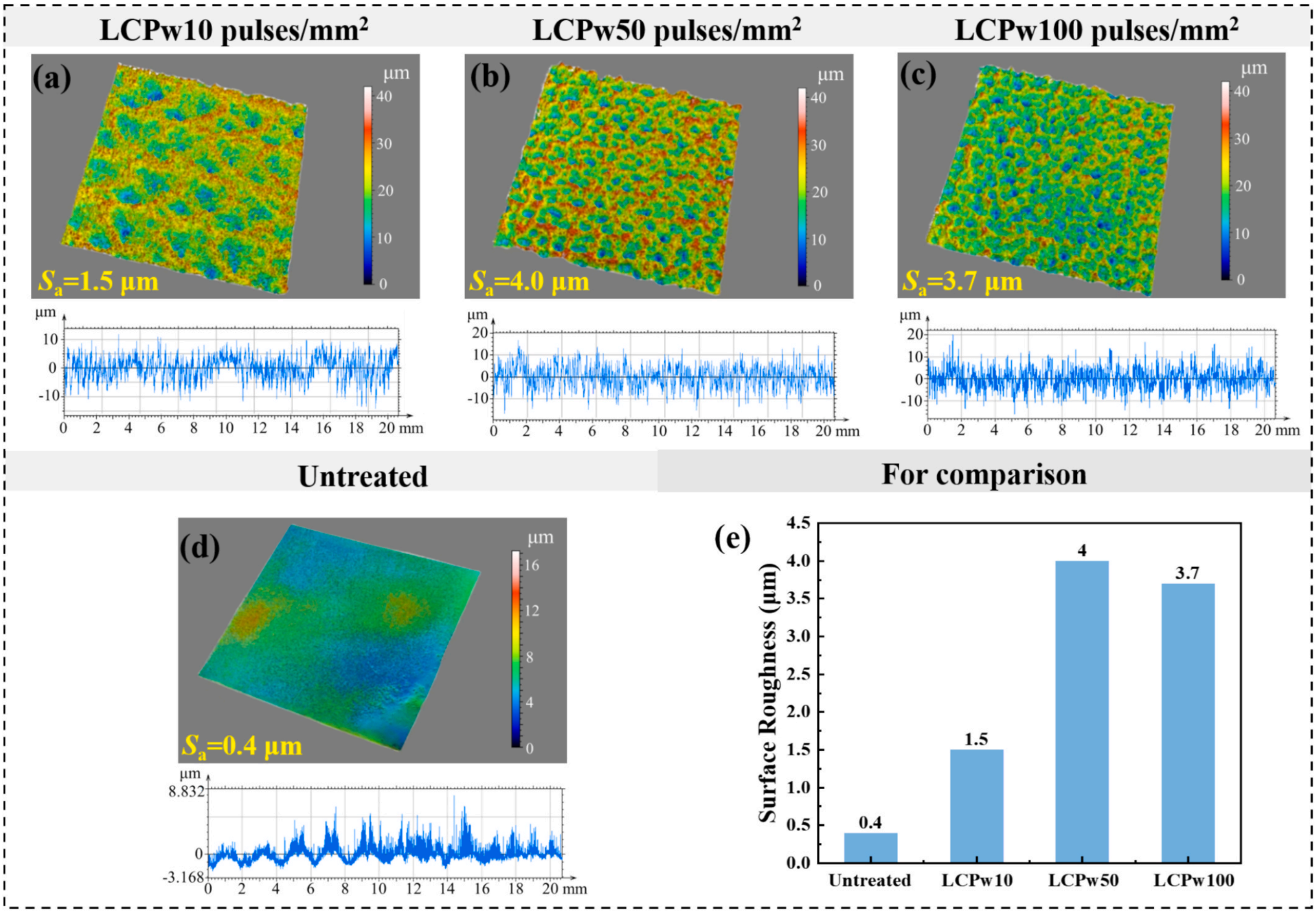

Fig. 6. Surface morphology and corresponding line profiles measured by confocal microscopy: (a) 10 pulses/mm^2, (b) 50 pulses/mm^2, (c) 100 pulses/mm^2, (d) untreated specimen, and (e) comparison of surface roughness at different pulse densities.

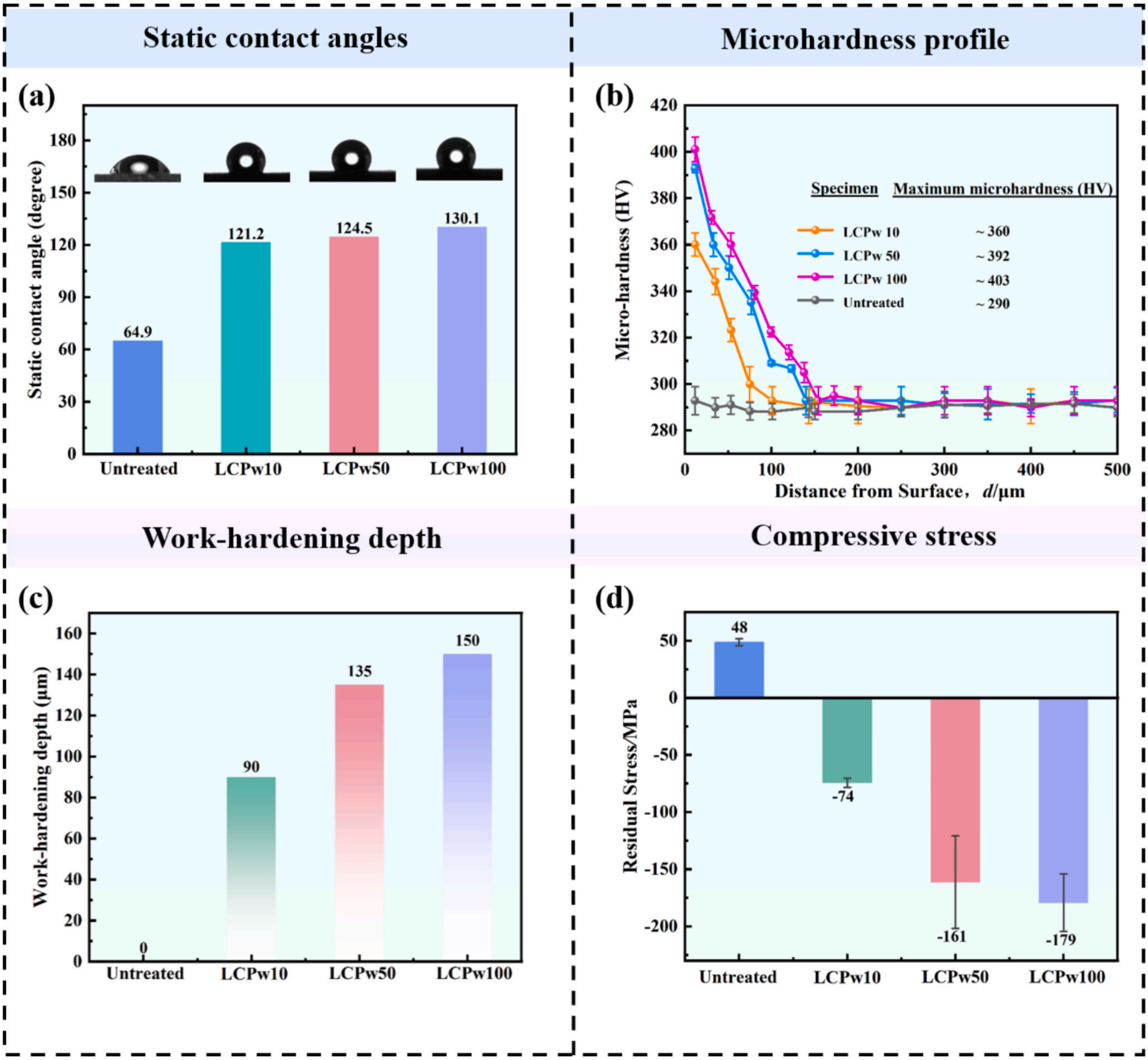

Fig. 7. Surface characteristics of the Ti–30Zr–5Mo alloy after LCPwC treatment at different pulse densities: (a) static contact angles of the untreated surface and the LCPwC-treated surfaces at 10, 50, and 100 pulses/mm^2; (b) microhardness depth profiles of the untreated and LCPwC-treated specimens; (c) work-hardening depths at different LCPwC pulse densities; and (d) surface residual stresses of the untreated and LCPwC-treated specimens measured by X-ray diffraction.

investigation. Since surface wettability can influence protein adsorption, cell attachment, and bacterial adhesion, the biological implications of this change should be further evaluated through dedicated in vitro and in vivo studies. Therefore, the overall biological performance of LCPwC-treated surfaces should be assessed in accordance with specific clinical requirements.

3.5. Microhardness and residual stress

Microhardness is an important indicator of resistance to elastic and plastic deformation and is closely related to wear resistance [42]. Microhardness depth profiles of the untreated and LCPwC-treated Ti–30Zr–5Mo specimens are shown in Fig. 7(b) and 7(c). The maximum surface microhardness increases from 290 HV for the untreated specimen to 360 HV at 10 pulses/mm^2 (24%), 392 HV at 50 pulses/mm^2 (35%), and 403 HV at 100 pulses/mm^2 (39%). Hardness gradually decreases with depth, reaching the untreated value (~290 HV) beyond the work-hardened layer, with effective work-hardening depths of 90, 135, and 150 μm for 10, 50, and 100 pulses/mm^2, respectively. This hardening may be attributed to plastic deformation, grain refinement, and increased dislocation density (Fig. 4) [43,44], with saturation at higher pulse densities limiting further hardening [45].

The residual stress, measured by X-ray diffraction, is 48 MPa for the untreated specimen and changes to −74, −161, and −179 MPa after LCPwC treatment at 10, 50, and 100 pulses/mm^2, respectively, as shown in Fig. 7(d). The increase in compressive stress with pulse density may result from a volumetric mismatch between the deformed surface and the unaffected substrate, together with dislocation motion and grain refinement associated with enhanced nucleation [46]. However, the increase in compressive stress from 50 to 100 pulses/mm^2 (11.1%) is limited by the plastic deformation capacity of the material, because saturation of dislocation networks and short-range recovery reduce further stress accumulation [47]. A higher pulse density enhances cavitation bubble collapse and generates stronger shock waves, which intensify plastic deformation and increase dislocation density (Fig. 4). This contributes to microstructural refinement, although the increase in residual compressive stress becomes less pronounced at higher pulse densities.

3.6. Dry sliding friction and wear properties

Wear resistance is a critical mechanical property for biomedical implants, as wear failure is a leading cause of implant degradation [45]. While laser shock peening enhances the wear resistance of Ti–6Al–4 V alloy [48], studies on laser cavitation peening without coating (LCPwC) for titanium alloys remain limited. Surface properties, including wettability, roughness, and microhardness, have a significant influence on friction and wear behavior [49,50]. This study evaluates the wear resistance of Ti–30Zr–5Mo alloy treated with LCPwC at a pulse density of 10 pulses/mm^2. This condition was selected because it provides a significant increase in microhardness (360 HV, Fig. 7(b)), moderate residual compressive stress (−74 MPa, Fig. 7(d)), a thicker oxide layer (3.9 μm, Fig. 3), and more efficient use of laser energy than higher pulse density conditions (50 and 100 pulses/mm^2). In this study, direct wear tests were limited to the 10 pulses/mm^2 condition. Although higher pulse densities (50 and 100 pulses/mm^2) further increase surface hardness, they also produce more severe cavitation-induced surface damage, higher roughness, and thinner oxide layers. These factors may compromise the mechanical stability of the surface during sliding and complicate the interpretation of wear behavior. In contrast, the specimen treated at 10 pulses/mm^2 provides a more balanced combination of hardness, residual compressive stress, oxide-layer thickness, and surface integrity. Accordingly, the 10 pulses/mm^2 condition was selected for subsequent wear testing.

The coefficient of friction (COF) curves are shown in Fig. 8(a). The untreated specimen exhibits a stable average COF of 0.56, whereas the LCPwC-treated specimen exhibits a much lower COF of 0.12. During the initial break-in period (0–10 min), the LCPwC-treated specimen exhibits fluctuations in COF because the initial contact area is relatively small and gradually increases with wear until a dynamic equilibrium is reached [16]. Despite increased roughness (S_a = 1.5 μm, Fig. 6) and hydrophobicity (121.2°, Fig. 7), the reduced COF suggests that the enhanced microhardness (360 HV, Fig. 7(b)) and residual compressive stress (−74 MPa, Fig. 7(d)) outweigh the adverse effect of increased roughness on frictional resistance. The harder surface improves resistance to abrasive wear, while the TiO_2-rich oxide layer (Fig. 5) may help reduce adhesive wear, thereby contributing to the low COF [51].

Confocal microscopy (Fig. 8(g, k)) shows that the wear track of the LCPwC-treated specimen is narrower and shallower than that of the untreated specimen. The two-dimensional cross-sectional profiles (Fig. 8(b)) reveal a maximum wear depth at the track center, with protrusions at the edges due to plastic flow and material pile-up resulting from compression and shear forces [52]. The LCPwC-treated specimen exhibits smoother wear profiles, indicating less severe material flaking compared to the pronounced fluctuations observed in the untreated specimen. Wear volume, calculated from confocal microscopy data, and wear mass, measured using an analytical balance with a resolution of 0.0001 g, are shown in Fig. 8(c). The LCPwC-treated specimen exhibits a 26.2% reduction in wear volume and a 50% reduction in wear mass compared to the untreated specimen.

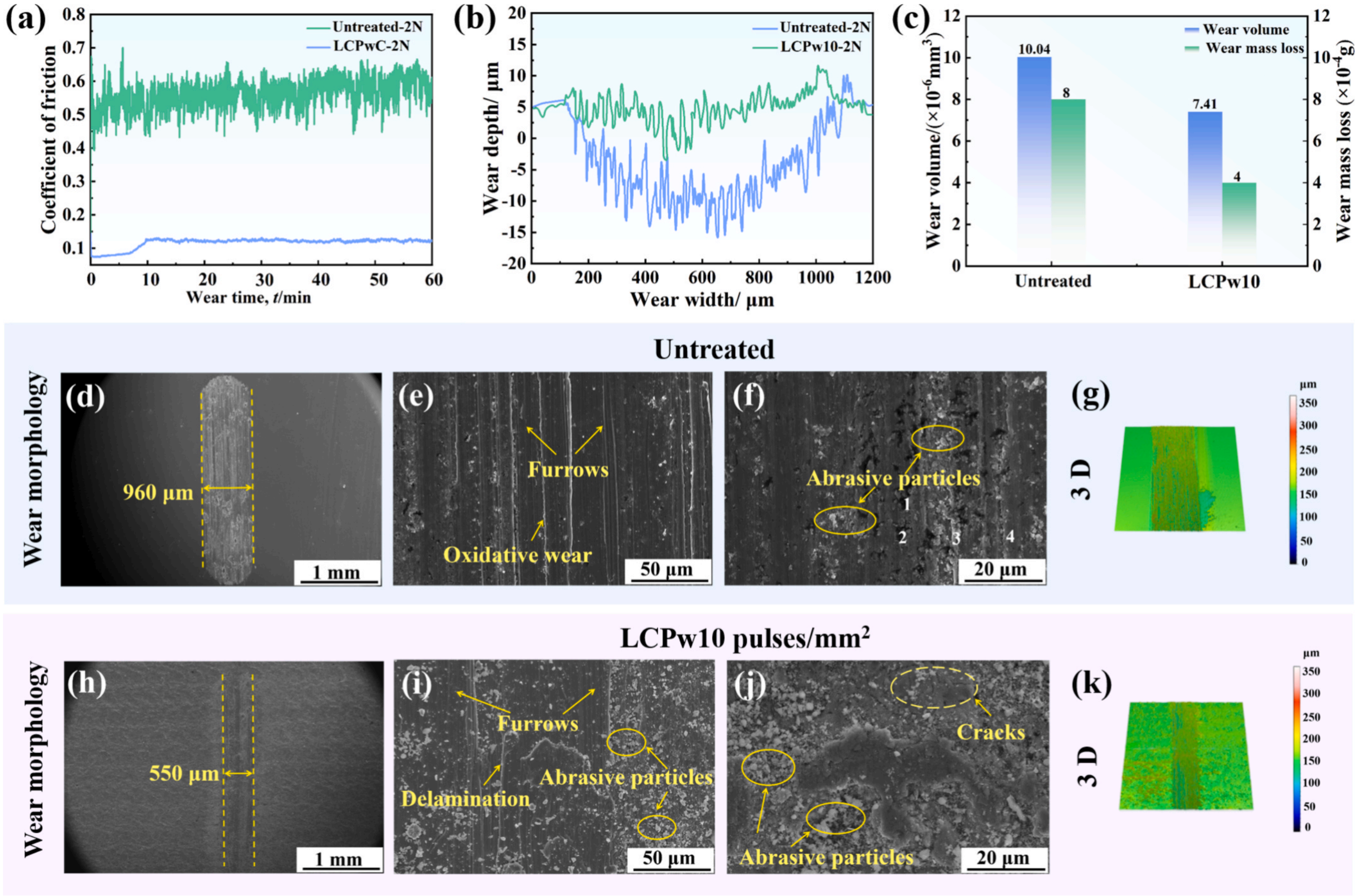

Fig. 8. Tribological behavior and wear characteristics of the Ti–30Zr–5Mo alloy before and after LCPwC treatment at 10 pulses/mm^2: (a) coefficient of friction (COF) curves of the untreated and LCPwC-treated specimens; (b) 2D cross-sectional wear profiles; (c) comparison of wear volume and mass loss; (d–f) wear surface morphology of the untreated specimen; (g) 3D wear-track morphology of the untreated specimen; (h–j) wear surface morphology of the LCPwC-treated specimen; and (k) 3D wear-track morphology of the LCPwC-treated specimen.

To elucidate the wear mechanism, the worn surfaces are analyzed using SEM, as illustrated in Fig. 8. The wear track of the untreated specimen (Fig. 8(d–f)) exhibits distinct furrows, fine scratches, and significant debris accumulation, indicating both abrasive and oxidative wear. EDS analysis (Table 1) shows the presence of oxygen on the untreated wear surface, suggesting oxidation during sliding [16]. In contrast, the LCPwC-treated specimen (Fig. 8(h–j)) exhibits a narrower wear track (550 μm), pronounced furrows, and reduced debris, with evidence of delamination and minor oxidation, suggesting that abrasive wear is the dominant wear mechanism. The LCPwC-treated specimen exhibits smaller flaking areas and numerous oxide chips (Fig. 8(j)), consistent with the higher hardness of the treated surface (360 HV, Fig. 7(b)) and its greater resistance to plastic deformation. Microcracks generated in the oxide layer by cavitation-induced stress (Fig. 3) may propagate under sliding stress, leading to local spallation and the formation of oxide chips that accumulate on the worn surface and act as a protective tribolayer, thereby limiting further wear propagation [51]. The TiO_2-rich oxide layer (Fig. 5) and moderate roughness ($S_a = 1.5$ μm, Fig. 6) may further reduce adhesive wear and thereby improve wear resistance.

4. Discussion

4.1. Oxide layer formation during LCPwC

The formation of an oxide layer on the Ti–30Zr–5Mo alloy during LCPwC is attributed to the synergistic interaction between the aqueous medium and the extreme thermo-mechanical conditions at the water–metal interface, as illustrated in Fig. 9(a). Upon focused laser irradiation, rapid vaporization of the adjacent water generates high-temperature plasma and cavitation bubbles [25]. The expansion and violent collapse of these bubbles generate shock waves that impose localized plastic deformation, cyclic loading, and transient heating on the alloy surface. In the absence of a protective coating, direct contact with water allows dissociation products, including •OH radicals, H^+, O_2^-, atomic oxygen, and molecular oxygen, to form through laser-induced plasma and thermal and pressure effects [36,53]. These reactive oxygen species create a transient oxygen-rich environment that can accelerate the oxidation of Ti and Zr. Concurrently, cavitation-induced pressure transients and microscale fluid motion enhance interfacial mass transport, thereby facilitating inward oxygen diffusion and the rapid formation of a dense surface oxide layer [54,55].

Consequently, water plays multiple important roles during LCPwC. It serves as the medium for plasma and cavitation bubble formation, the source of reactive oxygen species through laser-induced dissociation, and the facilitator of oxygen transport via hydrodynamic effects induced by bubble collapse. These coupled processes collectively contribute to the rapid in situ oxidation observed on the Ti–30Zr–5Mo alloy surface.

XPS analysis indicates that the oxide composition varies significantly with pulse density. At 10 pulses/mm^2, TiO_2 is the dominant oxide species (76.8%), whereas Ti_2O_3 is present only in a minor fraction (6.7%), owing to relatively high oxygen availability and a longer effective oxidation period. At 100 pulses/mm^2, the Ti_2O_3 fraction increases to 20.9%, whereas the TiO_2 fraction decreases to 56.9%, suggesting more limited oxygen availability and shorter effective reaction times under more intense cavitation. The variation in oxide composition can be interpreted in terms of oxygen partial pressure and reaction kinetics [56,57]. At low pulse densities, relatively high oxygen availability and sufficient diffusion favor the formation of fully oxidized TiO_2, which is thermodynamically stable under high oxygen potential. In contrast, higher pulse densities induce more intense cavitation, which may shorten the local oxygen residence time and restrict oxygen diffusion, thereby lowering oxygen partial pressure and stabilizing sub-stoichiometric oxides such as Ti_2O_3. In addition, the extremely rapid heating–cooling cycles inherent to laser cavitation may preserve metastable oxide phases formed under non-equilibrium conditions. ZrO_2 appears to form readily across all conditions, which may be related to the low oxidation enthalpy of Zr, with increased peak intensity at higher pulse densities [58]. These findings align with Kuji et al. [25], who attributed oxide formation to inward oxygen diffusion under laser irradiation. The oxide-layer thickness decreases from 3.9 μm at 10 pulses/mm^2 to 1.3 μm at 100 pulses/mm^2 (Fig. 3), which may be driven by stronger cavitation jets that remove nascent oxides at higher pulse densities. The oxide-layer thickness is therefore controlled by a dynamic balance between growth and removal processes. While the aqueous environment continuously supplies oxygen to drive oxidation, cavitation bubble collapse generates intense pressure fluctuations and near-surface shear forces that dislodge weakly bound oxide fragments, thereby preventing excessive thickening. This dynamic growth–removal equilibrium results in a relatively thin yet dense and adherent oxide layer.

Table 1
EDS elemental composition (wt.%) of Ti, Zr, Mo, O, Si, and C at positions 1, 2, 3, and 4 on the wear surface of the untreated Ti–30Zr–5Mo alloy, as shown in Fig. 8(f).

Area	Ti	Zr	Mo	O	Si	C
1	53.27	21.48	3.42	13.62	0.66	7.55
2	55.11	23.58	3.47	8.80	1.59	7.45
3	55.83	22.99	3.26	12.88	0.69	4.36
4	66.32	26.53	3.93	0	0	3.22

The microjet effect enhances interfacial mass transfer and local oxygen replenishment, thereby accelerating oxidation kinetics. Unlike conventional thermal oxidation or static liquid-phase oxidation, LCPwC induces a dynamic, non-equilibrium oxidation process characterized by high strain rates, a nanocrystalline structure, and a multiphase composition consisting of TiO_2, Ti_2O_3, and ZrO_2. This transient oxidation process, governed by pulse density, produces a gradient oxide layer that may be beneficial for improving the surface performance of Ti–30Zr–5Mo alloy in implant applications.

4.2. Effect of LCPwC on microstructure

XRD and EBSD analyses (Figs. 2 and 4) reveal significant microstructural changes associated with a partial α → β phase transformation in the surface of the Ti–30Zr–5Mo alloy after LCPwC. Unlike conventional heat treatment, this transformation may result from an adiabatic temperature rise caused by high-density plastic deformation during LCPwC. In contrast to laser shock peening, which employs an absorber layer, LCPwC's direct energy transfer induces intense non-uniform plastic flow via cavitation bubble collapse and shock-wave loading. The high dislocation density generates internal dissipation, converting plastic work into localized heat that accumulates adiabatically, potentially exceeding the β transus temperature (~700 °C for Ti–Zr–Mo alloys) before rapid cooling may stabilize the β-phase at room temperature [29].

The non-monotonic variation in grain size of the oxide layer, observed as 12.1, 9.1, and 9.5 nm, may be attributed to a grain evolution process primarily governed by the nucleation rate. At a low pulse density (10 pulses/mm^2), the limited number of heterogeneous nucleation sites, such as cavitation microcavities, interface cracks, and local chemical inhomogeneities, may reduce the nucleation rate. This allows ample space for grain growth, leading to a larger average grain size (12.1 nm). As pulse density increases to an intermediate level (50 pulses/mm^2), laser-induced cavitation and shock effects, coupled with instantaneous energy input, significantly enhance the density of nucleation sites. This promotes a higher nucleation rate, resulting in the formation of numerous grain nuclei with constrained growth, yielding the smallest grain size (9.1 nm). This behavior is consistent with a mechanism in which laser-induced cavitation promotes nucleation [59].

Similar nucleation-dominated refinement mechanisms are widely

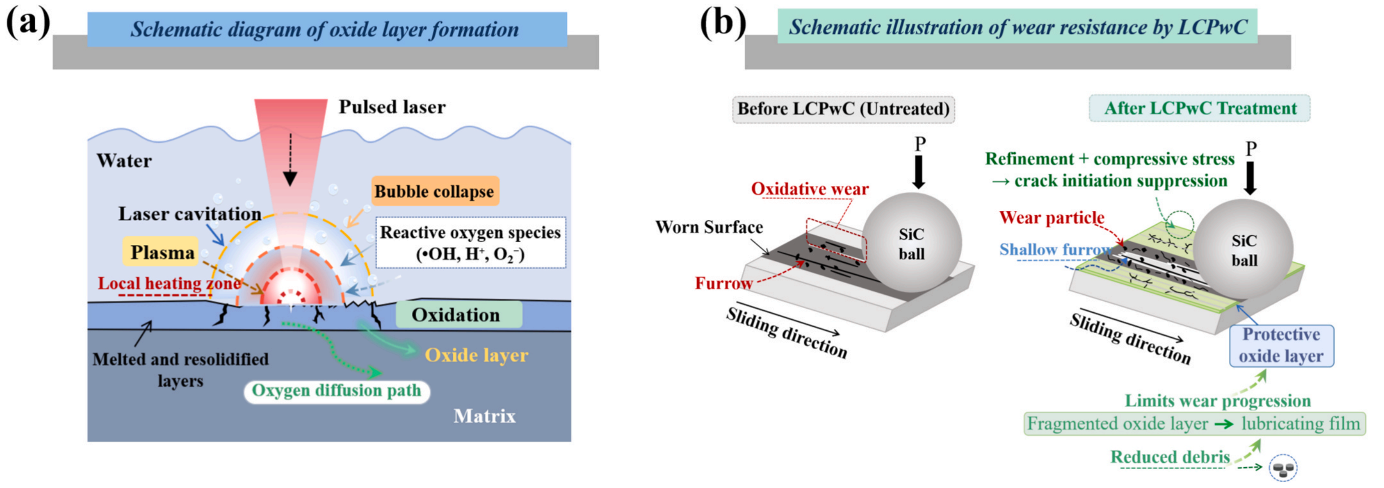

Fig. 9. Schematic illustrations showing (a) the oxide-layer formation mechanism during LCPwC and (b) the anti-wear mechanism of the Ti–30Zr–5Mo alloy before and after LCPwC treatment at 10 pulses/mm^2.

reported in high-strain-rate or laser-driven processes, where rapid dislocation and defect generation increase nucleation-site density and suppress grain coarsening, as observed in gradient nanograined metals [60]. Analogous non-monotonic grain-size evolution during laser processing has also been documented in nanocrystalline oxides and laser-modified metallic surfaces. For instance, in polycrystalline TiO_2 thin films, crystallite size initially increases and then decreases with prolonged laser irradiation, reflecting a shift from growth-dominated to defect-mediated refinement [61]. In contrast, in liquid-confined laser-irradiated titanium, the surface grain size initially decreases and then increases with increasing pulse number, as recovery and grain coalescence dominate at higher energy inputs [62]. These trends align with broader findings that ultrafast laser irradiation favors nucleation-dominated crystallization pathways while altering subsequent grain-growth kinetics [63]. As the pulse density further increases to 100 pulses/mm^2, the nucleation rate remains elevated, while local heat accumulation, short-range recovery, and subgrain coalescence collectively enable limited grain growth, resulting in a slight increase in the average grain size to 9.5 nm. This slight coarsening at higher pulse densities aligns with recovery- and recrystallization-assisted grain coalescence observed in nanosecond laser-irradiated TiO_2 nanoparticles, where localized heat accumulation activates defect annihilation and subgrain growth [64]. In addition, variations in pulse density affect the phase fractions of TiO_2, Ti_2O_3, and ZrO_2, as well as the distribution of surface defects, thereby further modulating the effectiveness of heterogeneous nucleation sites [65,66].

4.3. Antiwear mechanism of LCPwC

As discussed in Section 3.6, the Ti–30Zr–5Mo alloy treated with LCPwC at 10 pulses/mm^2 exhibits a prolonged break-in period and a significantly reduced coefficient of friction (COF, 0.12 vs. 0.56 for the untreated specimen, Fig. 8(a)), which may be attributed to LCPwC-induced changes in surface morphology, microhardness, and oxide-layer properties. In the untreated specimen, low roughness ($S_a = 0.4$ μm, Fig. 6) and hardness (290 HV, Fig. 7(b)) result in rapid COF stabilization during the break-in period [17]. LCPwC at 10 pulses/mm^2 increases the surface roughness to 1.5 μm (Fig. 6) and the microhardness by 24% to 360 HV (Fig. 7(b)). At the same time, the wear volume decreases by 26.2% (Fig. 8(c)), suggesting that the beneficial effect of enhanced hardness outweighs the adverse effect of increased roughness within this range.

Wear surfaces, analyzed by SEM (Fig. 8), reveal furrows and metallic debris in both untreated and LCPwC-treated specimens, indicating abrasive wear as a primary mechanism. EDS analysis (Table 1) reveals oxygen (0–13.62 wt%) on the untreated wear surface, suggesting the occurrence of oxidative wear. In contrast, the LCPwC-treated specimen exhibits reduced debris and oxide chip formation, suggesting a dominant abrasive mechanism with minor oxidation (Fig. 8(i–j)). LCPwC generates shock waves through cavitation bubble collapse (Fig. 9(a)), inducing severe plastic deformation and grain refinement (Fig. 4), which may contribute to the increase in surface hardness [67]. According to Archard's wear equation [68]:

$$V = K\frac{PL}{HV} \tag{3}$$

where V is wear volume (m^3), K is the dimensionless wear factor, P is the applied load (N), L is the sliding distance (m), and HV represents the Vickers hardness of the material (kgf/mm^2). Increased hardness reduces wear volume by enhancing load-bearing capacity and minimizing microscopic ploughing [19]. The wear factor K is also influenced by surface roughness (Fig. 6), oxide composition (Fig. 5), and wettability (water contact angle: 121.2°, Fig. 7), which collectively affect interfacial adhesion and wear behavior [49].

The TiO_2-rich oxide layer (76.8%, Fig. 5) formed at 10 pulses/mm^2 develops microcracks under cavitation-induced stress (Fig. 3), which can fragment during sliding to generate oxide chips that accumulate on the worn surface and act as a protective tribolayer, thereby limiting wear propagation (Fig. 8(j)). The subsurface grain refinement layer, supported by residual compressive stress (−74 MPa, Fig. 7(d)), enhances resistance to tensile cracking and plastic deformation under contact stresses, further reducing wear [46]. Surface wettability (Fig. 7) may also influence adhesive interactions during sliding [49]. These synergistic effects, including enhanced hardness, compressive stress, and a protective oxide layer, significantly improve wear resistance at 10 pulses/mm^2, as depicted in the anti-wear schematic (Fig. 9(b)). These results indicate that LCPwC is a promising strategy for improving the wear resistance of Ti–30Zr–5Mo alloy in implant applications.

5. Conclusion

This study investigates the surface oxidation and wear behavior of the Ti–30Zr–5Mo alloy after LCPwC treatment at pulse densities of 10, 50, and 100 pulses/mm^2. LCPwC improves the tribological performance of the alloy through a synergistic combination of oxide-layer formation, phase transformation, and mechanical property enhancement. The main findings are as follows:

(1) LCPwC induces the formation of a multiphase oxide layer (TiO_2, Ti_2O_3, and ZrO_2) and an $\alpha \rightarrow \beta$ phase transformation in the surface layer driven by adiabatic heating from shock-induced plastic deformation. The average grain size of the oxide layer decreases from 12.1 nm at 10 pulses/mm^2 to 9.1 nm at 50 pulses/mm^2, then slightly increases to 9.5 nm at 100 pulses/mm^2. At 100 pulses/mm^2, the oxide layer is thinner (1.3 μm), denser, and contains 20.9% Ti_2O_3.

(2) Surface roughness (S_a) increases from 0.4 μm (untreated) to 1.5 μm at 10 pulses/mm^2, 4.0 μm at 50 pulses/mm^2, and 3.7 μm at 100 pulses/mm^2 due to cavitation-induced micropits, followed by slight smoothing from oxide stripping. The water contact angle increases from 64.9° for the untreated specimen to 121.2°, 124.5°, and 130.1° at 10, 50, and 100 pulses/mm^2, respectively, indicating an increase in hydrophobicity.

(3) LCPwC increases surface microhardness to 360, 392, and 403 HV at 10, 50, and 100 pulses/mm^2, corresponding to increases of 24%, 35%, and 39%, respectively, with work-hardened layer thicknesses of 90, 135, and 150 μm. Residual compressive stresses reach −74, −161, and −179 MPa at 10, 50, and 100 pulses/mm^2, respectively, with a diminishing rate of increase at higher pulse density due to plastic deformation saturation.

(4) LCPwC at 10 pulses/mm^2 causes a 26.2% reduction in wear volume, a 50% reduction in wear mass, and a decrease in the coefficient of friction from 0.56 to 0.12. Enhanced hardness and a TiO_2-rich oxide layer act as a protective tribolayer, with abrasive wear as the dominant mechanism and minor oxidative wear also occurring.

(5) The above findings demonstrate that LCPwC significantly enhances the tribological performance of Ti–30Zr–5Mo alloy through a dense, multiphase oxide layer, increased microhardness, and residual compressive stress. This coating-free approach provides an effective strategy for improving wear resistance and modifying surface wettability in high-zirconium alloys, with potential relevance to implant applications.

CRediT authorship contribution statement

Ran Wang: Writing – original draft, Investigation, Conceptualization. **Hitoshi Soyama:** Writing – review & editing, Validation, Methodology. **Takayoshi Nakano:** Writing – review & editing, Validation, Funding acquisition. **Hideki Hosoda:** Writing – review & editing, Validation. **Mitsuo Niinomi:** Writing – review & editing, Validation. **Xiaowei Zhang:** Writing – review & editing, Validation. **Deliang Zhang:** Writing – review & editing, Validation. **Xiaoli Zhao:** Writing – review & editing, Writing – original draft, Supervision, Project administration, Methodology, Investigation, Funding acquisition.

Declaration of competing interest

The authors declare that they have no known competing financial interests or personal relationships that could have appeared to influence the work reported in this paper.

Acknowledgements

This work was financially supported by the National Natural Science Foundation of China (No. 52071068), the 111 Project, China (No. B16009) and JST-CREST (No. JPMJCR2194).

Data availability

The raw and processed data required to reproduce these findings are not publicly available due to their use in ongoing research. Data are available from the corresponding author upon reasonable request.

References

[1] W. Xiao, Y. Fu, J. Wang, D. Zeng, X. Liang, H. Chen, X. Zhao, C. Ma, Research progress in metastable β-type titanium alloys for biomedical applications, J. Mater. Eng. 51 (2023) 52–66, https://doi.org/10.11868/j.issn.1001-4381.2022.000545.

[2] X. Tang, T. Ahmed, H.J. Rack, Phase transformations in Ti–Nb–Ta and Ti–Nb–Ta–Zr alloys, J. Mater. Sci. 35 (2000) 1805–1811. https://doi.org/10.1023/A:1004792922155.

[3] E. Gemelli, N.H.A. Camargo, Oxidation kinetics of commercially pure titanium, Asian Chem. News. 12 (2007) 3, https://doi.org/10.1590/S1517-70762007000300014.

[4] T. Tanabe, M. Tomita, Surface oxidation of zirconium above room temperature, Surf. Sci. 222 (1989) 84–94, https://doi.org/10.1016/0039-6028(89)90336-1.

[5] W.F. Ho, C.P. Ju, J.H. Lin, Structure and properties of cast binary Ti–Mo alloys, Biomaterials 20 (1999) 2115–2122, https://doi.org/10.1016/S0142-9612(99)00114-3.

[6] X. Zhao, M. Niinomi, M. Nakai, G. Miyamoto, T. Furuhara, Microstructures and mechanical properties of metastable Ti–30Zr–(Cr, Mo) alloys with changeable Young's modulus for spinal fixation applications, Acta Biomater. 7 (2011) 3230–3236, https://doi.org/10.1016/j.actbio.2011.04.019.

[7] X. Zhao, M. Niinomi, M. Nakai, Relationship between various deformation-induced products and mechanical properties in metastable Ti–30Zr–Mo alloys for biomedical applications, J. Mech. Behav. Biomed. Mater. 4 (2011) 2009–2016, https://doi.org/10.1016/j.jmbbm.2011.06.020.

[8] X. Zhao, M. Niinomi, M. Nakai, T. Ishimoto, T. Nakano, Development of high Zr-containing Ti-based alloys with low Young's modulus for use in removable implants, Mater. Sci. Eng. C 31 (2011) 1436–1444, https://doi.org/10.1016/j.msec.2011.05.013.

[9] X. Zhao, Y. Wang, H. Xue, N. Jia, Y. Liu, D. Zhang, The effect of strain rate on deformation-induced α′ phase transformation and mechanical properties of a metastable β-type Ti–30Zr–5Mo alloy, J. Alloys Compd. 894 (2022) 162394, https://doi.org/10.1016/j.jallcom.2021.162394.

[10] X. Zhao, R. Zhu, W. Song, L. Meng, M. Niinomi, T. Nakano, N. Jia, D. Zhang, A strategy to regulate the yield ratio of a metastable high Zr-containing β titanium alloy: synergistic effects of the β domain, β stability and β/α interfaces by varying the α phase content, J. Alloys Compd. 952 (2023) 170024, https://doi.org/10.1016/j.jallcom.2023.170024.

[11] C. Wu, X. Zhao, M. Zhang, H. Hosoda, T. Nakano, M. Niinomi, N. Jia, Z. Shao, D. Zhang, Strong grain size effect on tensile behavior of the body-centered-cubic Ti–30Zr–5Mo alloy with stress-induced α′ martensitic transformation, Mater. Sci. Eng. A 900 (2024) 146455, https://doi.org/10.1016/j.msea.2024.146455.

[12] Y. Jin, J. Li, T. Nakano, H. Hosoda, M. Niinomi, X. Zhang, D. Zhang, X. Zhao, Zr-enhanced ambient-air thermal oxidation of Ti–30Zr–5Mo alloy using low T_β for implants, Mater. Today Commun. (2025) 113442, https://doi.org/10.1016/j.mtcomm.2025.113442.

[13] J. Xu, J. Zhang, Y. Shi, J. Tang, D. Huang, M. Yan, M.S. Dargusch, Surface modification of biomedical Ti and Ti alloys: a review on current advances, Mater 15 (2022) 1749, https://doi.org/10.3390/ma15051749.

[14] Y. Wang, X. Wang, C. Xu, S. Qiu, K. Wang, K. Tian, B. Yu, Y. Yu, Effect of shot peening and nitrogen ion implantation on the fatigue behavior of TA15 titanium alloys, Int. J. Fatigue 172 (2023) 107649, https://doi.org/10.1016/j.ijfatigue.2023.107649.

[15] M. Nair, S. Swaroop, Influence of oxide layer developed by laser shock peening on biocorrosion response of Ti–6Al–7Nb in simulated body fluid, Surf. Coat. Technol. 483 (2024) 130795, https://doi.org/10.1016/j.surfcoat.2024.130795.

[16] K. Luo, S. Xu, L. Xu, Y. Xing, H. Zhang, C. Wang, J. Lu, Wear behaviors of AISI 316L stainless steel with a gradient structured surface layer induced by laser shock peening, Surf. Coat. Technol. 481 (2024) 130608, https://doi.org/10.1016/j.surfcoat.2024.130608.

[17] D. Zhu, X. He, L. Zhong, G. Wang, G. Wei, G. Pang, W. Liao, Effect of laser shock peening on tribological properties of 55SiMoVA bearing steel, Opt. Laser Technol. 181 (2025) 111704, https://doi.org/10.1016/j.optlastec.2024.111704.

[18] S.H. Chang, Z.Y. Li, Effect of oxidation at an elevated temperature on the evolution of phases, microstructure, and properties of the oxide films formed on the surface of TiZr, Sci. Rep. 13 (2023) 5126, https://doi.org/10.1038/s41598-023-32377-y.

[19] M. Ge, J. Xiang, Y. Tang, X. Ye, Z. Fan, Y. Lu, X. Zhang, Wear behavior of Mg–3Al–1Zn alloy subjected to laser shock peening, Surf. Coat. Technol. 337 (2018) 501–509, https://doi.org/10.1016/j.surfcoat.2018.01.043.

[20] X. Shen, P. Shukla, F. Yao, S. Nath, Z. An, J. Lawrence, Laser shock peening of orthopaedic Ti–6Al–7Nb: evaluation of topography, wetting characteristics, microstructure and residual stress, Int. J. Peen. Sci. Technol. 1 (2) (2019) 137–154. https://www.oldcitypublishing.com/journals/ijpst-home/ijpst-issue-contents/ijpst-volume-1-issue-2-2018/ijpst-1-2-p-137-154/.

[21] H. Soyama, A.M. Korsunsky, A critical comparative review of cavitation peening and other surface peening methods, J. Mater. Proc. Technol. 305 (2022) 117586, https://doi.org/10.1016/j.jmatprotec.2022.117586.

[22] J. Gu, Z. Hu, H. Zhu, D. Lu, Effect of laser cavitation peening on surface integrity and electrochemical corrosion behavior of magnesium alloy, Mater. Today Commun. 38 (2024) 107806, https://doi.org/10.1016/j.mtcomm.2023.107806.

[23] J. Gu, C. Luo, P. Ma, X. Xu, Y. Wu, X. Ren, Study on processing and peening mechanisms of mild steel subjected to laser cavitation peening, Appl. Surf. Sci. 562 (2021) 150242, https://doi.org/10.1016/j.apsusc.2021.150242.

[24] J. Gu, C. Luo, P. Zhang, P. Ma, X. Ren, Laser cavitation peening of grey cast iron: effect of coverage layer on the surface integrity, Appl. Surf. Sci. 521 (2020) 146295, https://doi.org/10.1016/j.apsusc.2020.146295.

[25] C. Kuji, H. Soyama, Mechanical surface treatment of titanium alloy Ti6Al4V manufactured by direct metal laser sintering using laser cavitation, Metals 13 (2023) 181, https://doi.org/10.3390/met13010181.
[26] H. Soyama, K.L. Wong, D. Eakins, A.M. Korsunsky, The effects of submerged laser peening, cavitation peening, and shot peening on the improvement of the torsional fatigue strength of powder bed fused Ti6Al4V produced through laser sintering, Inter. J. Fatigue. 185 (2024) 108348, https://doi.org/10.1016/j.ijfatigue.2024.108348.
[27] Z. Zhang, S. Wei, P. Wang, W. Qiu, G. Zhang, Progress in applications of laser-induced cavitation on surface processing, Opt. Laser Technol. 170 (2024) 110212, https://doi.org/10.1016/j.optlastec.2023.110212.
[28] X. Ren, J. Wang, S. Yuan, S. Adu-Gyamfi, Y. Tong, C. Zuo, H. Zhan, Mechanical effect of laser-induced cavitation bubble of 2A02 alloy, Opt. Laser Technol. 105 (2018) 180–184, https://doi.org/10.1016/j.optlastec.2018.02.039.
[29] A. Umapathi, S. Swaroop, Deformation of single and multiple laser peened TC6 titanium alloy, Opt. Laser Technol. 100 (2018) 309–316, https://doi.org/10.1016/j.optlastec.2017.10.022.
[30] Z. Niu, H. Men, C. Wang, P. Gai, W. Zhou, G. Chen, Z. Fang, X. Fu, Effect of surface high density twin microstructure induced by shot peening on the fatigue behavior of Ti–6Al–4V, J. Mater. Res. Technol. 30 (2024) 1806–1821, https://doi.org/10.1016/j.jmrt.2024.03.234.
[31] J.I. Langford, A.J.C. Wilson, Scherrer after sixty years: a survey and some new results in the determination of crystallite size, J. Appl. Crystallogr. 11 (2) (1978) 102–113, https://doi.org/10.1107/S0021889878012844.
[32] T. Zhou, Y. Xiong, Z. Chen, X. Zha, Y. Lu, T. He, F. Ren, H. Singh, J. Kömi, M. Huttula, W. Cao, Effect of surface nano-crystallization induced by supersonic fine particles bombarding on microstructure and mechanical properties of 300M steel, Surf. Coat. Technol. 421 (2021) 127381, https://doi.org/10.1016/j.surfcoat.2021.127381.
[33] G. Wang, S. Luo, Y. Guo, R. Huang, C. Wang, Z. Qu, Investigating the correlation between mechanical properties and gradient microstructures in laser shock peened CrCoNi alloy, Int. J. Plast 189 (2025) 104331, https://doi.org/10.1016/j.ijplas.2025.104331.
[34] A.A. Bugayev, M.C. Gupta, R. Payne, Laser processing of Inconel 600 and surface structure, Opt. Lasers Eng. 44 (2) (2006) 102–111, https://doi.org/10.1016/j.optlaseng.2005.04.014.
[35] W.M. Al Qahtani, C. Schille, S. Spintzyk, M.S. Al Qahtani, E. Engel, J. Geis-Gerstorfer, F. Rupp, L. Scheideler, Effect of surface modification of zirconia on cell adhesion, metabolic activity and proliferation of human osteoblasts, Biomed Tech (Berl) 62 (2017) 75–87, https://doi.org/10.1515/bmt-2015-0139.
[36] J. Gu, C. Luo, Z. Lu, P. Ma, X. Xu, X. Ren, Bubble dynamic evolution, material peening and chemical effect induced by laser cavitation peening, Ultrason. Sonochem. 72 (2021) 105441, https://doi.org/10.1016/j.ultsonch.2020.105441.
[37] M. Kong, T. Zang, Z. Wang, L. Zhu, H. Zheng, S. Gao, H.M. Ngwangwa, A study on the tribological behavior of AZ31 magnesium alloy sheets processed by temperature-assisted ultrasonic shot peening, J. Mater. Res. Technol. 27 (2023) 1223–1241, https://doi.org/10.1016/j.jmrt.2023.09.293.
[38] S. Velayuthaperumal, R. Radhakrishnan, Effect of different laser texture configurations on improving surface wettability and wear characteristics of Ti6Al4V implant material, J. Braz. Soc. Mech. Sci. Eng. 45 (2023) 363, https://doi.org/10.1007/s40430-023-04287-7.
[39] P. Li, S. Wang, K. Yu, L. Zhang, Y. Jiang, G. Wang, Superhydrophobic biomimetic microstructures prepared by laser-ablation for drag reduction, Colloids Surf A Physicochem Eng Asp 686 (2024) 133381, https://doi.org/10.1016/j.colsurfa.2024.133381.
[40] M. Abeens, R. Muruganandhan, K. Thirumavalavan, Effect of low energy laser shock peening on plastic deformation, wettability and corrosion resistance of aluminum alloy 7075 T651, Optik 219 (2020) 165045, https://doi.org/10.1016/j.ijleo.2020.165045.
[41] S. Prabhakaran, A. Kulkarni, G. Vasanth, S. Kalainathan, P. Shukla, V. K. Vasudevan, Laser shock peening without coating induced residual stress distribution, wettability characteristics and enhanced pitting corrosion resistance of austenitic stainless steel, Appl. Surf. Sci. 428 (2018) 17–30, https://doi.org/10.1016/j.apsusc.2017.09.138.
[42] J. Fu, Y. Zhu, C. Zheng, R. Liu, Z. Ji, Effect of laser shock peening on mechanical properties of Zr-based bulk metallic glass, Appl. Surf. Sci. 313 (2014) 692–697, https://doi.org/10.1016/j.apsusc.2014.06.056.
[43] S.A. Kumar, S.G.S. Raman, T.S.N.S. Narayanan, R. Gnanamoorthy, Influence of counterbody material on fretting wear behaviour of surface mechanical attrition treated Ti–6Al–4V, Tribol. Int. 57 (2013) 107–114, https://doi.org/10.1016/j.triboint.2012.07.021.
[44] S. Mironov, T. Onuma, Y.S. Sato, S. Yoneyama, H. Kokawa, Tensile behavior of friction-stir welded AZ31 magnesium alloy, Mater. Sci. Eng. A 679 (2017) 272–281, https://doi.org/10.1016/j.msea.2016.10.036.
[45] X. Shen, P. Shukla, S. Nath, J. Lawrence, Improvement in mechanical properties of titanium alloy (Ti–6Al–7Nb) subject to multiple laser shock peening, Surf. Coat. Technol. 327 (2017) 101–109, https://doi.org/10.1016/j.surfcoat.2017.08.009.
[46] G. Luo, L. Zhang, Y. Xiong, B. Zhang, X. Chen, Y. Wu, S. Wang, W. Cao, Effect of laser shock peening on the corrosion properties of Ti–6Al–3Nb–2Zr–1Mo alloy, Surf. Coat. Technol. 440 (2022) 128425, https://doi.org/10.1016/j.surfcoat.2022.128425.
[47] X. Nie, W. He, L. Zhou, Q. Li, X. Wang, Experiment investigation of laser shock peening on TC6 titanium alloy to improve high cycle fatigue performance, Mater. Sci. Eng. A 594 (2014) 161–167, https://doi.org/10.1016/j.msea.2013.11.073.
[48] C. Gu, Z. Tian, J. Zhao, Y. Wang, Investigation of microstructure and tribological property of Ti–6Al–4V alloy by laser shock peening processing, Int. J. Adv. Manuf. Technol. 129 (2023) 955–967, https://doi.org/10.1007/s00170-023-12354-5.
[49] Y. Han, F. Liu, K. Zhang, Q. Huang, X. Guo, C. Wang, A study on tribological properties of textured Co–Cr–Mo alloy for artificial hip joints, Int. J. Refractory Metals Hard Mater. 95 (2021) 105463, https://doi.org/10.1016/j.ijrmhm.2020.105463.
[50] T. Pratap, K. Patra, Tribological performances of symmetrically micro-textured Ti–6Al–4V alloy for hip joint, Int. J. Mech. Sci. 182 (2020) 105736, https://doi.org/10.1016/j.ijmecsci.2020.105736.
[51] Q. Zeng, S. Sun, Z. Pang, X. Wei, Study on high-temperature, ultra-low wear behaviors of Ti6Al4V alloy with thermal oxidation treatment, Coatings 14 (2024) 416, https://doi.org/10.3390/coatings14040416.
[52] R. Jiang, S. Zhang, X. Qin, R. Wang, M. Zhang, Z. Zhang, W. Zhang, Improving the wear resistance of Ti–6Al–4V alloy through electro-pulsing combined with laser shock peening, J. Mater. Res. Technol. 31 (2024) 1945–1955, https://doi.org/10.1016/j.jmrt.2024.06.213.
[53] Y. Du, N.A. Deskins, Z. Zhang, Z. Dohnálek, M. Dupuis, I. Lyubinetsky, Imaging consecutive steps of O_2 reaction with hydroxylated TiO_2 (110): Identification of HO_2 and terminal OH intermediates, J. Phys. Chem. C 113 (2) (2009) 666–671, https://doi.org/10.1021/jp807030n.
[54] D.F. Gaitan, L.A. Crum, C.C. Church, R.A. Roy, Sonoluminescence and bubble dynamics for a single, stable, cavitation bubble, J. Acoust. Soc. Am. 91 (1992) 3166–3183, https://doi.org/10.1121/1.402855.
[55] I. Tomashchuk, N. Zaitseva, M.C. Marco de Lucas, L. Postec, J.-M. Jouvard, L. Lavisse, Influence of aqueous environment on nanosecond laser modification of titanium surfaces, Appl. Phys. A 131 (2025) 1020, https://doi.org/10.1007/s00339-025-09140-3.
[56] S.V. Bulyarskiy, G.G. Gusarov, D.A. Koiva, G.A. Rudakov, Effect of oxygen partial pressure on the stoichiometric composition of titanium oxide films during magnetron sputtering, Phys. Solid State 63 (2021) 1611–1618, https://doi.org/10.1134/S1063783421100061.
[57] J.L. Murray, H.A. Wriedt, The O–Ti (Oxygen–Titanium) system, Bull. Alloy Phase Diagr. 8 (1987) 148–165, https://doi.org/10.1007/BF02873201.
[58] R. Coloma Ribera, R.W.E. van de Kruijs, J.M. Sturm, A.E. Yakshin, F. Bijkerk, Intermixing and thermal oxidation of ZrO_2 thin films grown on α-Si, SiN, and SiO_2 by metallic and oxidic mode magnetron sputtering, J. Appl. Phys. 121 (2017) 115303, https://doi.org/10.1063/1.4978367.
[59] A. Soare, R. Dijkink, M.R. Pascual, C. Sun, P.W. Cains, D. Lohse, A.I. Stankiewicz, H.J.M. Kramer, Crystal nucleation by laser-induced cavitation, Cryst. Growth Des. 11 (6) (2011) 2311–2316, https://doi.org/10.1021/cg2000014.
[60] Y. Liu, J. Yu, G. Wu, Z. Zhang, D. Lu, Z. Zhang, H. Huang, L. Li, Grain refinement mechanism in gradient nanostructured Mg–Gd–Y–Zn–Zr alloy prepared by severe shear deformation, Mater. Sci. Eng. A 894 (2024) 146207, https://doi.org/10.1016/j.msea.2024.146207.
[61] M.I. Khan, A. Ali, Effect of laser irradiation on the structural, morphological and electrical properties of polycrystalline TiO_2 thin films, Results Phys. 7 (2017) 3455–3458, https://doi.org/10.1016/j.rinp.2017.09.005.
[62] N. Ali, S. Bashir, U. Kalsoom, M.S. Rafique, D. Yousaf, S. Ahmad, Effect of laser pulses on the surface and structural modification of ablated titanium in a liquid-confined environment, Radiat Eff. Defects Solids 170 (2015) 121–129, https://doi.org/10.1080/10420150.2014.998672.
[63] J. Yu, J. Yan, X. Li, L. Qu, Progress in ultrafast laser-induced nucleation and crystal growth, Zhongguo Jiguang/chinese Journal of Lasers. 48 (2021) 0202020, https://doi.org/10.3788/CJL202148.0202020.
[64] M. Soleimani, M. Nankali, W. Duley, X. Zhao, P. Peng, Y.N. Zhou, Ultra-low-temperature sintering of TiO_2 via grain boundary diffusion enabled by nanosecond laser irradiation, Mater. Today Nano 33 (2026) 100732, https://doi.org/10.1016/j.mtnano.2025.100732.
[65] O. Van Overschelde, R. Snyders, M. Wautelet, Crystallisation of TiO_2 thin films induced by excimer laser irradiation, Appl. Surf. Sci. 254 (4) (2007) 971–974, https://doi.org/10.1016/j.apsusc.2007.08.018.
[66] J.S. Hoppius, D. Bialuschewski, S. Mathur, A. Ostendorf, E.L. Gurevich, Femtosecond laser crystallization of amorphous titanium oxide thin films, Appl. Phys. Lett. 113 (7) (2018) 071904, https://doi.org/10.1063/1.5027899.
[67] Y. Liu, B. Jin, D. Li, X. Zeng, J. Lu, Wear behavior of nanocrystalline structured magnesium alloy induced by surface mechanical attrition treatment, Surf. Coat. Technol. 261 (2015) 219–226, https://doi.org/10.1016/j.surfcoat.2014.11.026.
[68] J.F. Archard, Contact and rubbing of flat surfaces, J. Appl. Phys. 24 (1953) 981–988, https://doi.org/10.1063/1.1721448.